Planar velocity measurements in compressible mixing layers

Article *in* Journal of Fluid Mechanics · March 2001

DOI: 10.1017/S0022112000003177

2 authors, including:

Godfrey Mungal
Stanford University
218 PUBLICATIONS **4,609** CITATIONS

Planar Velocity Measurements in Compressible Mixing Layers

Paper AIAA 97-0757: 35th Aerospace Sciences Meeting, Reno, NV

W. D. Urban* and M. G. Mungal†

Mechanical Engineering Department
Stanford University, Stanford, CA 94305-3032

Experimental considerations and preliminary results for PIV velocity field measurements in compressible gaseous mixing layers are presented. Particular attention is given to tracer particle selection and characterization. Experimental measurements of the velocity relaxation time downstream of an oblique shock are presented for two candidate seed particles, permitting a performance-based selection to be made. The chosen particles are then used to obtain side-view velocity measurements of a compressible mixing layer at a convective Mach number of 0.63. Preliminary observations regarding the velocity field are presented, along with interpretation in light of scalar visualizations obtained in previous work. Regions of fluid having velocities near the freestream values are found to persist well into the layer, with spatial variations reminiscent of the topology of the large-scale structures. This suggests that the momentum transfer is driven by the fluid's interaction with the structures, rather than by its initial entrainment into the layer. Contours of velocity magnitude are used to provide a scalar view of the data, and instantaneous and frame-averaged cross-stream velocity profiles are presented.

Nomenclature

Roman characters

a	Sound speed
C	Dimensionless coefficient
d	Diameter
F	Force
Kn	Knudsen number
$\dot{m}$	Mass flow rate
M	Mach number
m.p.	Melting point
P	Pressure
r	Velocity ratio
Re	Reynolds number
s	Density ratio
SG	Specific gravity
St	Stokes number
T	Temperature
U	Freestream or structure velocity
u	Streamwise velocity component
v	Cross-stream velocity component
x	Streamwise coordinate
y	Cross-stream coordinate

Greek characters

δ	Mixing layer thickness
Δt	Laser pulse separation
μ	Dynamic viscosity
ρ	Density
τ	Characteristic time

Sub- and superscripts

1	High-speed stream
2	Low-speed stream
c	Convective
cl	Centerline
d	Based on particle diameter
D	Drag
eff	Effective
ex	Nozzle exit
f	Fluid-mechanical
img	At imaging station
mat	Particle material
nom	Nominal
p	Particle
s	Stokes flow
vis	Visual

*Student Member AIAA
†Associate Professor, Senior Member AIAA

Introduction

The compressible mixing layer has received considerable attention in recent years, since it presents fundamental flow features present in many engineering systems, offers a wide parameter space, and lends itself well to both numerical and experimental analysis. Since the exploratory study by Papamoschou and Roshko [26], experimental efforts have concentrated on the study of the individual and combined effects of compressibility, density ratio, and heat release on the velocity and scalar fields of the flow, as well as the efficacy of various enhancement techniques. Scalar imaging has produced both flow visualization [3, 7, 21] and quantitative mixing data [16]. With the extension to double-pulsed illumination, successive scalar visualizations have been obtained, permitting calculation of large-scale structure convection velocities for both nonreacting [25, 11, 8, 28] and reacting [32] layers. Multi-component velocity measurements have been performed in mixing layers using laser-Doppler velocimetry (LDV) [6, 13, 14], generating mean profiles as well as turbulence statistics on a pointwise basis. The extension to planar velocity measurement in the compressible mixing layer has centered on the use of filtered Rayleigh velocimetry [9, 10]. The present technique, particle image velocimetry (PIV), has seen supersonic application in jets [17, 18, 33], wakes [24], and external flows [4]. The issue of tracer selection and delivery initially arose in connection with LDV experiments [15], and has since been extended to PIV [24]. Numerous investigators [30, 19] have demonstrated the technique of measuring particle response using wedge-generated shocks. In the present work, we seek to apply instantaneous, two-component, planar velocity measurement via PIV to the compressible mixing layer. In order to maximize the accuracy and to aid the interpretation of the results, we begin by validating the performance of our velocimeter, with special attention to seed-particle dynamics.

Experimental Apparatus

Wind Tunnel

The flow facility (Figure 1) is a blow-down wind tunnel used for supersonic mixing and combustion experiments [3, 22]. Two independent flow metering systems supply gas (in the present experiments, air) from pressurized tanks to a pair of plenums. After passing through perforated plate and honeycomb flow-conditioning elements, the high- and low-speed flows are accelerated into the test section by supersonic and subsonic nozzles respectively. At the end of the nozzles, the splitter plate separating the two streams tapers to a tip, resulting in a plane shear layer 10 cm wide in the test section. The test section is 8 cm high and 48 cm long, and operates at 0.6–0.8 atm. The discharge pressures of the nozzles are matched at the beginning of the test section by regulating the mass flow rates of the two streams, and the streamwise pressure gradient is minimized through adjustment of the upper and lower test section walls. Quartz windows provide optical access on all four sides of the test section. The shear layer compressibility, parametrized by the convective Mach number M_c, is varied by changing the nozzle contour, and hence the exit Mach number, of the supersonic stream. A 1 MW hydrogen-fueled vitiation heater upstream of the high-speed plenum allows heating of the supersonic stream to stagnation temperatures up to 1800 K, either to provide an ignition source for a reacting mixing layer [23, 22] or to raise the high-speed freestream velocity at a fixed Mach number. The present study (Table 1) uses ambient stagnation temperature and a high-speed Mach number of 2.25 to generate a compressible layer at $M_c = 0.63$. Higher compressibilities may be obtained either through operation of the vitiation heater or by using a heavy gas in the low-speed stream. Experiments are computer-sequenced, and last approximately 30 s from beginning to end, with data taken during a 10–20 s steady-state period. A nitrogen gas purge retards ambient condensation on external window surfaces during the experiment.

Imaging and PIV Analysis System

The PIV data acquisition system appears in Figure 2. Illumination is provided by a Quanta-Ray PIV-400 pulsed Nd:YAG laser. The laser contains two independent cavities whose IR beams are polarization combined before entering a shared frequency-doubling crystal, resulting in collinear beams of 532 nm light at up to 400 mJ per laser per 8 ns pulse. Output from the laser is formed into a sheet by means of cylindrical expansion and focusing lenses. The two realizations necessary for PIV are obtained by firing the two cavities sequentially, with a typical pulse separation Δt of 630 ns. The need for double pulses of high spatial and temporal quality at such short values of Δt recommends the

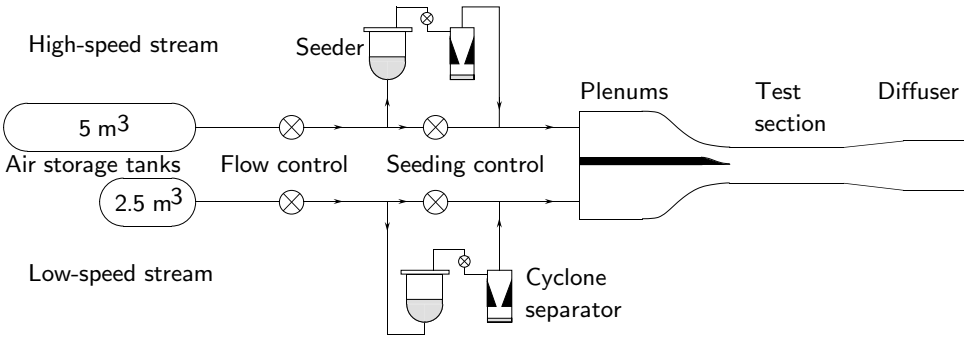

Figure 1: Supersonic mixing layer facility

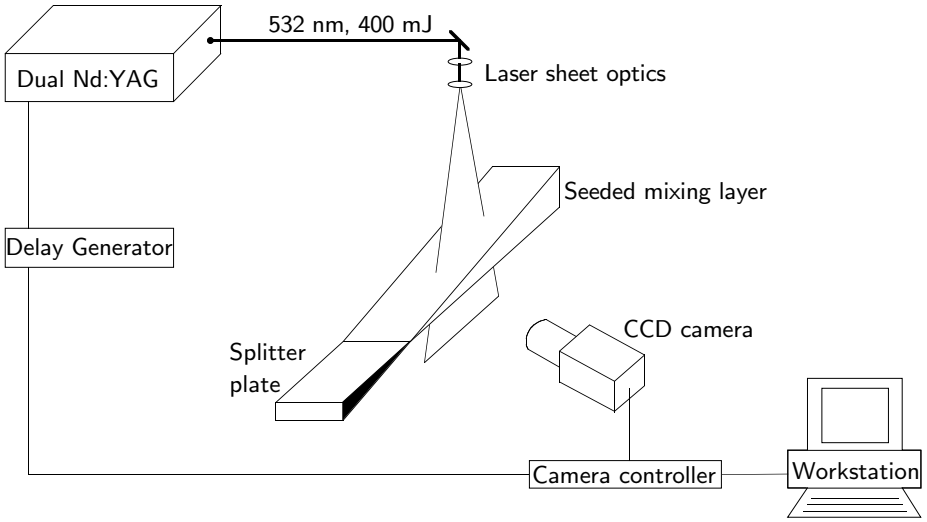

Figure 2: Component schematic for PIV measurements of the supersonic mixing layer

Case	$M_c = 0.63$	
Stream	1	2
M_{ex}	2.18	0.51
M_{img}	2.22	0.54
U_{img} [m/s]	519	173
a_{img} [m/s]	234	320
T_{img} [K]	136	255
P_{img} [kPa]	67	70
$\dot{m}$ [kg/s]	2.2	0.74
$r \equiv U_2/U_1$	0.33	
$s \equiv \rho_2/\rho_1$	0.53	
x_{img} [cm]	29	
$\delta_{vis,img}$ [cm]	2.1	
$Re_{\delta,img}/1000$	764	

Table 1: Mixing layer conditions

dual-cavity laser over a single-cavity double-pulsed unit for high-speed applications. Scattering from the particles is collected at 90° from a 48×24 mm region of the flow by a 2000×2000 pixel Kodak Megaplus 4.2 CCD camera equipped with a Nikkor 105 mm $f/2.8$ lens normally set to $f/5.6$. The low aspect ratio of the region of interest permits acquisition of double-exposed images at up to 1.5 Hz, since only half of the array is used. A readout error originating in the frame-grabber and affecting alternating columns is corrected in post-processing. Velocity vectors are calculated on an IBM RS 6000 workstation by means of an FFT-based autocorrelation. Interrogation regions are 80 pixels square, and peaks in the autocorrelation function are localized using a Gaussian curve fit. Since there are no velocity reversals in the lab frame in this flow, no biasing or tagging is necessary to resolve directional ambiguity.

Experimental Considerations

Since PIV measures the velocity of the tracer particles rather than the fluid itself, the measurement accuracy would depend on the behavior of the seed even if one were to track individual particle pairs. In practice, however, each measurement is based on an ensemble of particles whose displacement is recorded optically and inferred statistically, so the image density and signal-return characteristics of the seed particles influence the accuracy and facility of the measurement as well. Furthermore, an approach to the seeding problem must consider not only the tracer-particle material but also the means by which it is delivered. Thus, the suitability of a seeding scheme for a particular application is a composite of the following elements:

1. The ability of the seeding system to deliver the seed to the region of interest in the proper density and size distribution;
2. The ability of the seed to follow the flow; and
3. The ability of the imaging and analysis system to record and vectorize a field of particle images.

High-velocity flows are especially demanding, due to spatial variations in density, which complicate item (1), and steep velocity gradients, which challenge item (2). In this section, we begin with a general discussion of seed-particle selection, then individually address the three criteria enumerated above.

Seed Particle Selection

Criteria bearing on our seed selection included flow-following ability, monodispersity, pressure and temperature envelope, health hazard, and cost. Solid tracer particles were chosen to preserve the option of heating the high-speed freestream, as well as to permit injection at our high plenum pressures (up to 10 atm—beyond the range of commercial jet atomizers). A survey of available metal oxide particles appears in Table 2. Since the flow rates of the wind tunnel result in seed consumption of approximately 0.25 kg per run, cost was an important constraint in the final decision. The 0.3 μm alumina (Al_2O_3) from Praxair and the 0.015 μm titanium dioxide (TiO_2) from Tioxide were used in the comparison experiments described below. It should be noted that the manufacturers' nominal sizing for both products is somewhat misleading. The alumina particles are actually fairly widely dispersed [5], and readily agglomerate into larger clumps. In the case of the TiO_2, the 15 nm figure refers to a 'fundamental' particle size, with actual samples consisting of indivisible agglomerates approximately ten times larger. The fundamental particle size serves mainly to distinguish this product, an 'ultra-fine' grade, from the less-expensive 0.23 μm-nominal material, which in practice agglomerates to yet larger sizes. For particles in this size range, a rule of thumb is that agglomeration serves to increase the effective particle size by about an order of magnitude. Therefore, to achieve the

Vendor	Material	d_{nom} [μm]	SG_{mat}	SG_{eff}	τ_p [μs]	\$/kg	Comments
Aremco	Al_2O_3	0.85	3.97	3.97	14	73.85	
Aremco	MnO_2	0.9	5.03	5.03	19	88.18	
Aremco	MoS_2	0.9	4.80	4.80	18	78.59	
Aremco	TiO_2	0.65	4.05	4.05	8.6	17.97	
Aremco	$ZrSiO_4$	0.85	4.55	4.55	16	51.23	m.p. = 2550°C
C.E.D.	SiO_2	2.6	2.3	2.3	65	0.71	'Cristobalite'
Osaka Gas	SiO_2	1.0	2.3	0.45	2.1	19500	Manufactured
Osaka Gas	SiO_2	2.7	2.3	0.45	14	19500	Manufactured
Polar Minerals	$BaSO_4$	0.9	4.3	4.3	16	—	
Praxair	Al_2O_3	0.3	3.97	3.97	2.3	121.	
Sigma	Talc	0.4	3.2	3.2	3.0	34.59	
Sphere Services	SiO_2	10	2.3	0.7	28	—	Coal ash
Tioxide	TiO_2	0.015	4.05	4.05	8.2 ns	22.40	
Tioxide	TiO_2	0.23	4.05	4.05	1.6	2.76	
TSI	TiO_2	0.2	4.05	4.05	1.3	242.	

Table 2: Survey of solid metal oxide particles

submicron sizes desired in the test section, it was necessary, as we shall see, to specify the ultra-fine powder.

Flow Seeding Hardware

Each seeder is a 10–25-cm deep fluidized bed contained in a pressure vessel [5, 27]. The seeder diameters are chosen so that the fluid velocity through the bed is high enough to fluidize the required amount of seed, yet low enough that only the smallest particles are entrained. The channeling and slugging instabilities common to fluidized beds are minimized through frequent agitation by means of a rotating impeller within the bed.

In order to address the particle agglomeration which plagues velocimetry with solid seeds, hydrodynamic cyclones [27, 30] are placed between the seeder outlets and the injection point. The cyclones are sized according to a set of scaling rules [2] which relate all secondary cyclone dimensions to the diameter of the cylindrical upper section, which in turn depends upon the desired cutoff size through a geometry-dependent correlation for inertial separation [34]. Our cyclones were designed for a 50% cutoff size of around 0.3 μm for particles with specific gravities near 4; experience with the relative rejection rates of the two particles considered in this study suggests that the cyclones are operating near design conditions.

A butterfly valve in each flow train generates the pressure drop necessary to divert approximately 5% of the flow through the seeding systems, while smaller globe valves between each seeder and its cyclone permit fine control over the seeding levels. After seeding, the carrier gas is re-mixed with the bulk flows via transverse injection 2–3 m upstream of the plenums. Injection at this location eliminates post-conditioning disturbances, allows thorough mixing of the seeded carrier stream with the bulk flow, and ensures that the entire test section is seeded. The last feature improves the uniformity of seeding in the imaging plane, and simplifies changes of viewing field or angle.

Particle Dynamics

Consideration of seed-particle dynamics is especially important in PIV measurements in high-speed flows, since large velocity gradients challenge the flow-following capability of all but the smallest particles, and spatial variations in density make it difficult to establish uniformly satisfactory seeding levels. Additionally, particles lagging high-speed vortical flows will be expelled from the vortices, forming preferential concentration patterns apart from the fluid density field [12, 36]. As has been observed for LDV [31], and as we shall see for PIV, the statistical distribution of particle sizes can couple with the sensitivity of the imaging system to introduce still further effects. Finally, we note that conditions for particle lag are dependent not only on the particles and the integral-scale behavior of the fluid but also on the relationship between spatial variations in fluid velocity and the resolution of the imaging system. It has been noted [29] that the particles need only track the velocity variations from one PIV interrogation region to another, and that gradients within the regions too steep for the particles to follow will nevertheless be reflected

faithfully in the average value reported for the region. For the present experiment, however, we have still attempted to optimize particle performance to ensure that our spatial resolution is sensor-limited rather than particle-limited.

Theoretical Background

Particle-dynamic effects are normally parametrized by the Stokes number St, the ratio of characteristic particle time τ_p to the time scale τ_f of the flow variations to be measured. For effective flow following at the scale represented by τ_f, we require that $St \ll 1$. The particle time is the $1/e$ time constant for a particle to react to a step input in relative velocity. If the relative velocity is small ($Re_d \ll 1$), the flow is incompressible ($M \ll 1$), and the particles are significantly larger than the mean free path in the gas ($Kn_d \ll 1$), then the familiar Stokes drag law applies:

$$F_D = 3\pi\mu U d \tag{1}$$

Solving the equation of motion for the step response of a particle to a change in fluid velocity leads to an exponential response with characteristic time

$$\tau_\mathrm{p} = \frac{\rho_\mathrm{p} d_\mathrm{p}^2}{18\mu} \tag{2}$$

Equation 1 is customarily recast in pseudo-inertial terms as

$$C_{D,\mathrm{s}} = \frac{24}{Re_d} \tag{3}$$

which is subjected to inertial, compressibility, and free-molecule corrections before recalculating τ_p via the linearized relation

$$\tau_\mathrm{p} = \frac{\rho_\mathrm{p} d_\mathrm{p}^2}{18\mu} \frac{C_{D,\mathrm{s}}}{C_D} \tag{4}$$

where C_D is now the modified drag coefficient. Walsh [35] provides an exhaustive comparison of various C_D formulations with data, but in the present case (low relative Mach and Reynolds numbers, but very small particles), a simple correction for free-molecule flow is adequate [20]:

$$C_D = \frac{24}{Re_d(1 + 2.7Kn_d)} \tag{5}$$

which leads to

$$\tau_\mathrm{p} = \frac{\rho_\mathrm{p} d_\mathrm{p}^2}{18\mu}(1 + 2.7Kn_d) \tag{6}$$

For the present experiment, the integral-scale fluid-mechanical time, given by $\delta/\Delta U$, is approximately $60\,\mu$s. Therefore, for satisfactory flow-following we seek a particle with τ_p below $10\,\mu$s. Applying Equation 6 to the nominal properties of our candidate particles, we arrive at unrealistically low τ_p estimates of $2.3\,\mu$s for the Al_2O_3 and 8.2 ns for the TiO_2. The objective of our particle-lag experiments, then, is to measure τ_p, and to calculate an effective particle diameter from it, and in turn to use this to identify and characterize an acceptable seed. The strong influence of particle diameter on particle dynamics suggested by Equation 6 motivates us to make this measurement in our test section, under conditions similar to those in our mixing layer experiments.

Particle Relaxation Experiments

The experiments consist of measurements of particle lag downstream of a two-dimensional oblique shock. Changes in the seed particles and the optical arrangement lead to estimates of the magnitude and variability of particle-dynamic effects. The high-speed stream of the mixing layer facility is used to provide a supersonic ($M = 2.2$) approach flow, and an oblique shock is generated by a two-dimensional 10° wedge mounted on the top wall of the tunnel. Representative particle images using the two seeds appear in Figure 3; the wedge appears at the top of the images and flow is from left to right. The mixing layer, which forms the lower boundary of the high-speed freestream, is visible at the bottom of the figures. Several qualitative features of these images suggest the superiority of the TiO_2 seed. First, we note that the Al_2O_3 image contains a greater number of vertical, dagger-like particle images. These 'bloomed' particle images result when overflowing charge due to saturation bleeds among adjacent pixels during readout of the CCD array; the saturation in turn results from the high signal returned by oversized particles in the flow. Thus, the readout blooming is an indication of the dispersion of the Al_2O_3 seed to larger sizes than the TiO_2. Another qualitative observation is that the TiO_2 seed visualizes the shock, while the Al_2O_3 seed does not. Since rapid, small-scale particle motion is required for a fluid density change to be reflected as a seeding density change, this suggests that the TiO_2 particles more faithfully follow the flow across the shock.

Analysis of the wedge-flow particle images leads

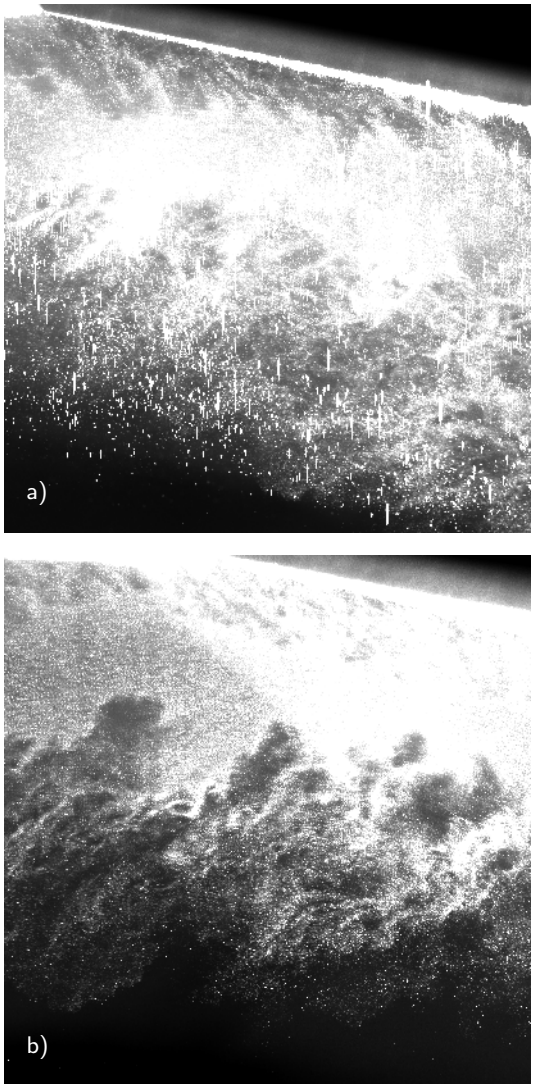

Figure 3: Wedge flow particle images for (a) Al_2O_3 and (b) TiO_2 seed particles

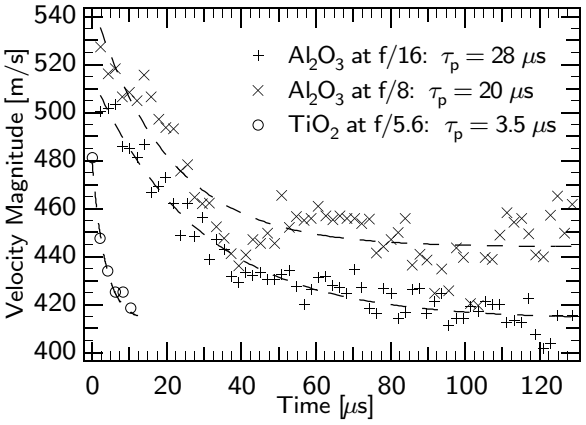

Figure 4: Wedge flow particle relaxation traces for Al_2O_3 and TiO_2 seed particles

to measurements of cross-shock velocity profiles for the two seeds (Figure 4). By transforming the spatial coordinate to time and applying exponential fits, we estimate τ_p to be 20–28 μs for the Al_2O_3 seed and 3.5 μs for the TiO_2 seed, translating to effective diameters of 1.2 and 0.4 μm respectively. These measurements agree well with the scattering-based measurements of Crosswy [5]. A final piece of evidence supporting the performance of the TiO_2 seed may be found in particle images from the mixing layer itself (Figure 5). In the first image, the lagging alumina seed forms preferential concentration patterns which mark the large scale structure of the layer, while in the second the TiO_2 seed is far more resistant to ejection from the vortices. In summary, the TiO_2 seed best satisfies our specifications with regard to particle-dynamic performance, cost, and ease of handling, so it is chosen for the mixing-layer measurements.

Imaging System Effects

Figure 4 displays two relaxation traces for the Al_2O_3 seed, corresponding to two sensitivities of the imaging system. This illustrates the bias that can afflict velocity measurements using polydisperse seed containing an appreciable fraction of particles too large to follow the subject flow. This phenomenon, previously observed in LDV studies, is illustrated schematically in Figure 6. Size distributions for the two particles considered are depicted, along with cubic curves [1] representing the response of the imaging system as a function of particle size, averaged over the area of the particle im-

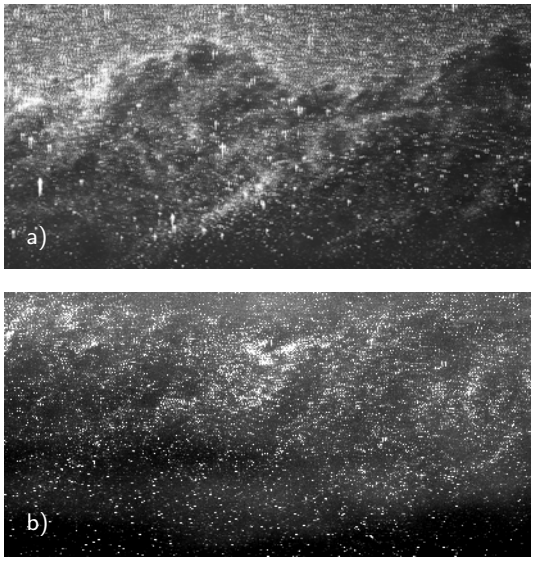

Figure 5: Mixing layer particle images for (a) Al_2O_3 and (b) TiO_2 seed particles

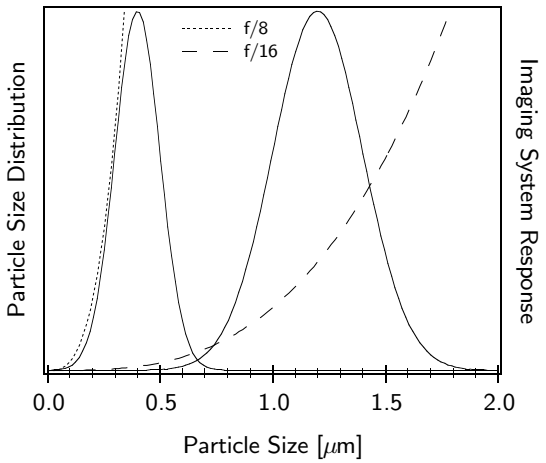

Figure 6: Illustration of flow-following bias due to seed size distribution

age. The latter determine the detection threshold of the imaging system, which may lie above, below, or within the particle size distribution. This threshold may be shifted along the particle-size spectrum by alteration of the laser fluence, optical collection efficiency, or imaging medium sensitivity. In the present experiments, the threshold was moved across the particle size distributions by varying the etendue of the collection lens. At $f/8$, the entire distribution of both particles lies above the detection threshold, and PIV measurements are possible. When the aperture is reduced to $f/16$, however, the TiO_2 particles are no longer visible; furthermore, only the *largest* Al_2O_3 particles are detected. This results in a measurement based upon the members of the distribution least able to follow the flow, and an increase in observed τ_p. Although an intermediate value of the sensitivity might place the threshold within the TiO_2 size distribution, little or no bias would result since the entire distribution lies at smaller particle sizes.

Mixing Layer PIV Measurements

Overview

This section presents preliminary velocity measurements in the compressible ($M_c = 0.63$) mixing layer described in Table 1. Velocity vectors were calculated on a 50 × 25 grid, yielding 50% overlap of the interrogation regions; for clarity, we show every third vector in the streamwise direction. The field of view encompasses the full width of the mixing layer, with small regions of freestream velocity on the high- and low-speed interfaces, and extends from $x = 26.5$ to $x = 31.5$ cm from the splitter tip. Flow is from left to right, and the fast stream is on the top. The Reynolds number $Re_\delta = \Delta U \delta/\nu$ is 764,000. A representative instantaneous velocity vector field for the mixing layer, derived from Figure 5b, is presented in Figure 7. Figure 8 shows the same data in a convective reference frame moving downstream at 375 m/s. Figures 9 and 10 are the corresponding average vector fields obtained from a 100-frame ensemble. Next, Figures 11 and 12 display the instantaneous (again, from Figure 5b) and average velocity magnitude fields. Finally, instantaneous and average cross-stream velocity profiles appear in Figures 13 and 14, with the average plotted against similarity coordinates in Figure 15.

Discussion

The instantaneous velocity field (Figure 7) displays a meandering pattern due to variations in the cross-stream (v) velocity. The spatial frequency of these variations (about $3\,\mathrm{cm}^{-1}$) is similar to that of the large-scale structures observed in scalar visualizations [3]. Similarly, the cross-stream profiles exhibit considerable variation from one streamwise realization to another, with distinct cross-stream movement of the inflection point, and, in some cases, local minima. One result of this variation is that the instantaneous boundaries of the layer at

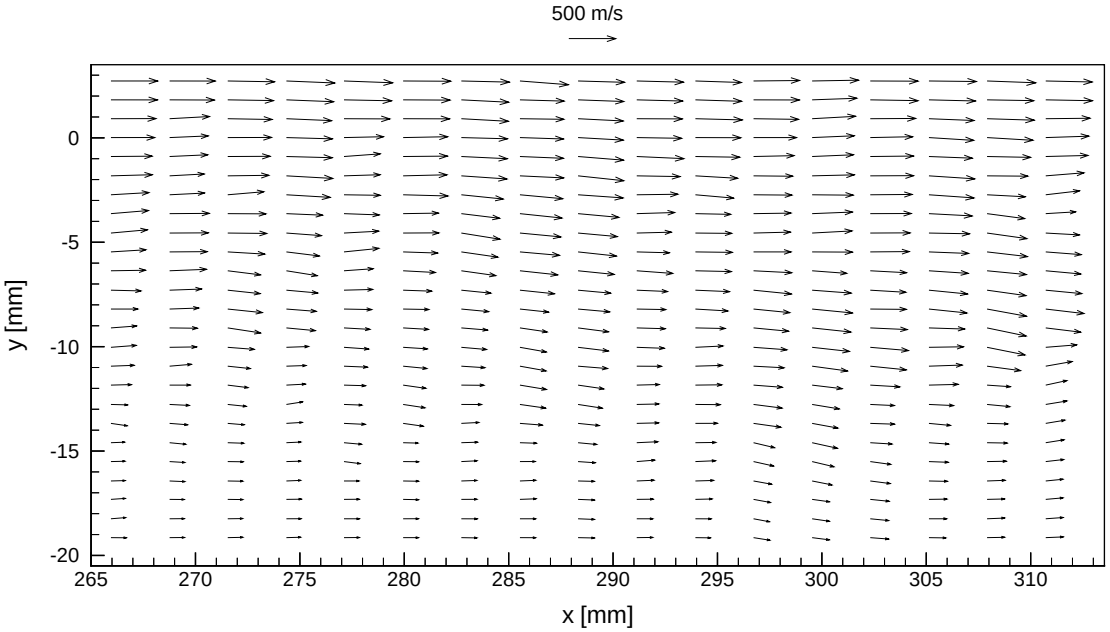

Figure 7: Instantaneous velocity field: $M_c = 0.63$

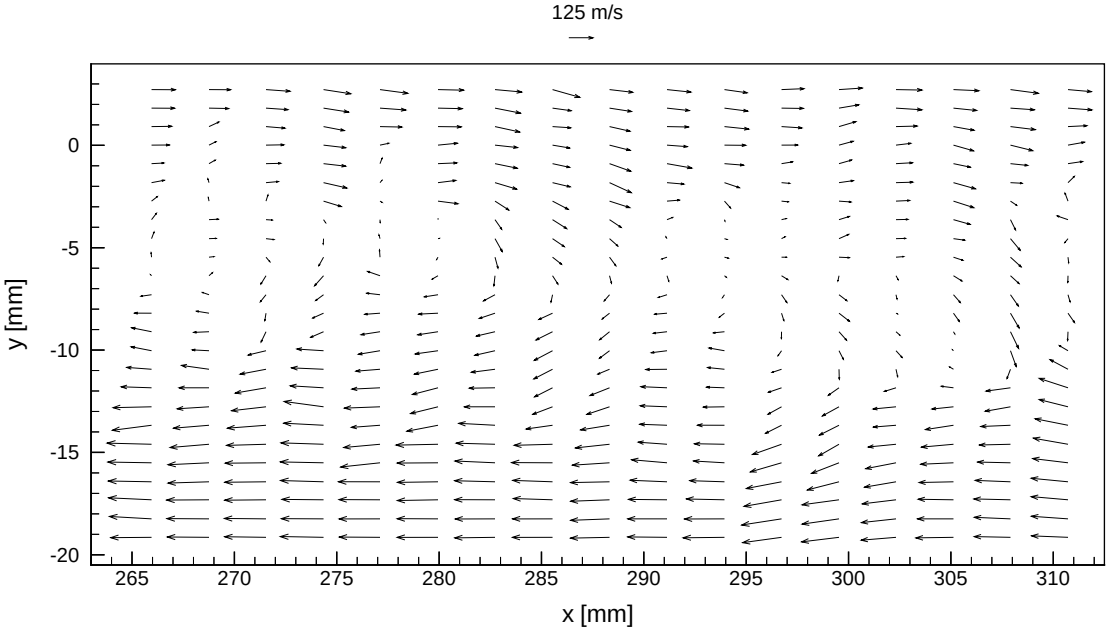

Figure 8: Instantaneous velocity field: $M_c = 0.63$, 375 m/s bias

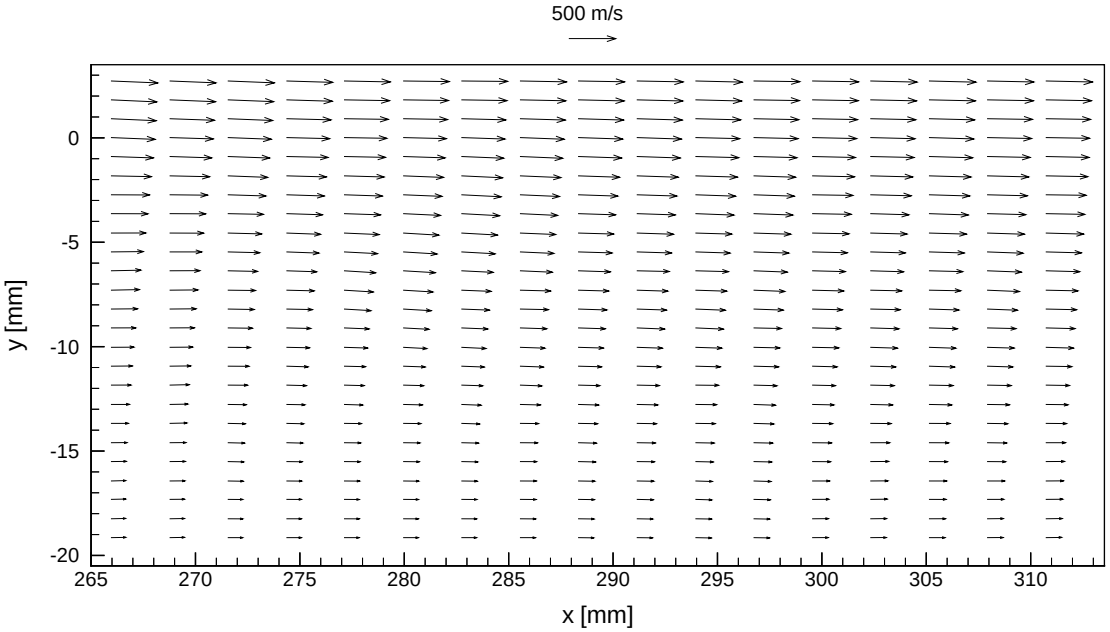

Figure 9: 100-frame average velocity field: $M_c = 0.63$

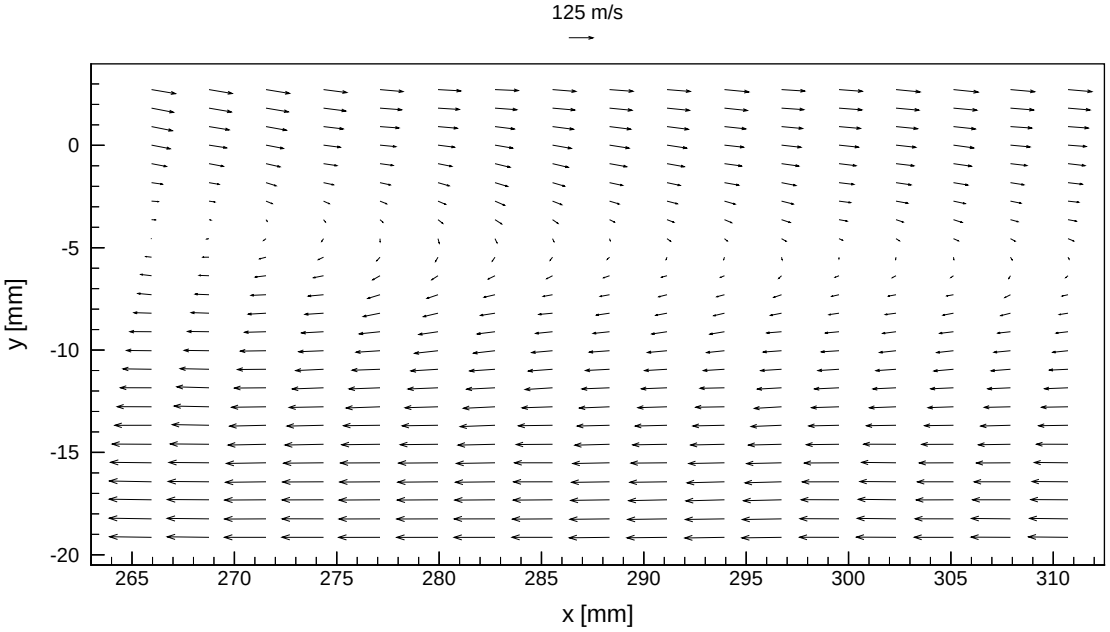

Figure 10: 100-frame average velocity field: $M_c = 0.63$, 375 m/s bias

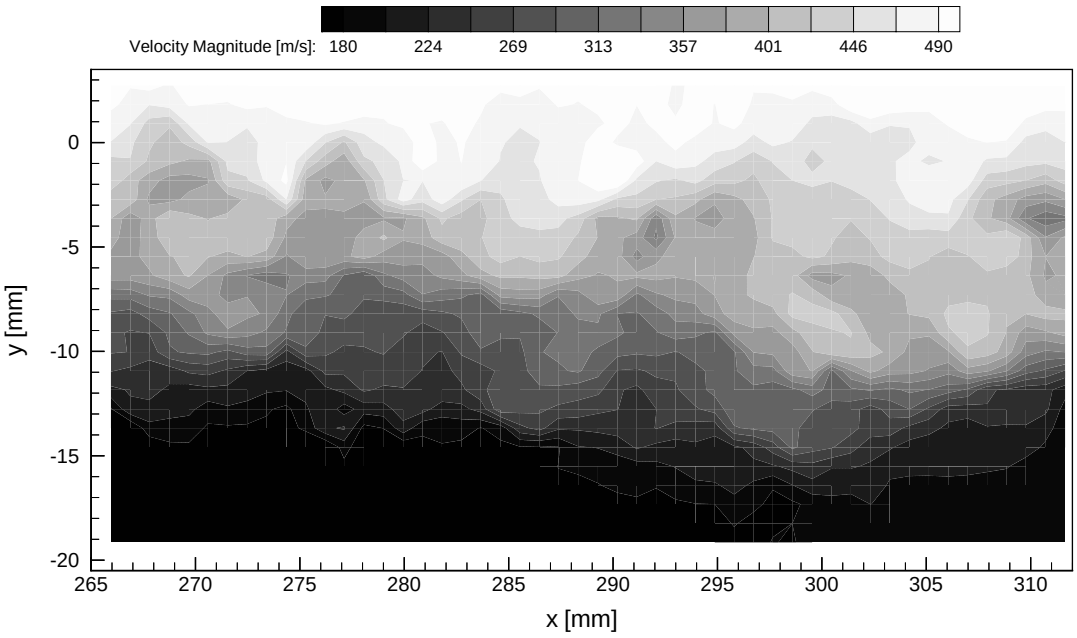

Figure 11: Instantaneous velocity magnitude: $M_c = 0.63$

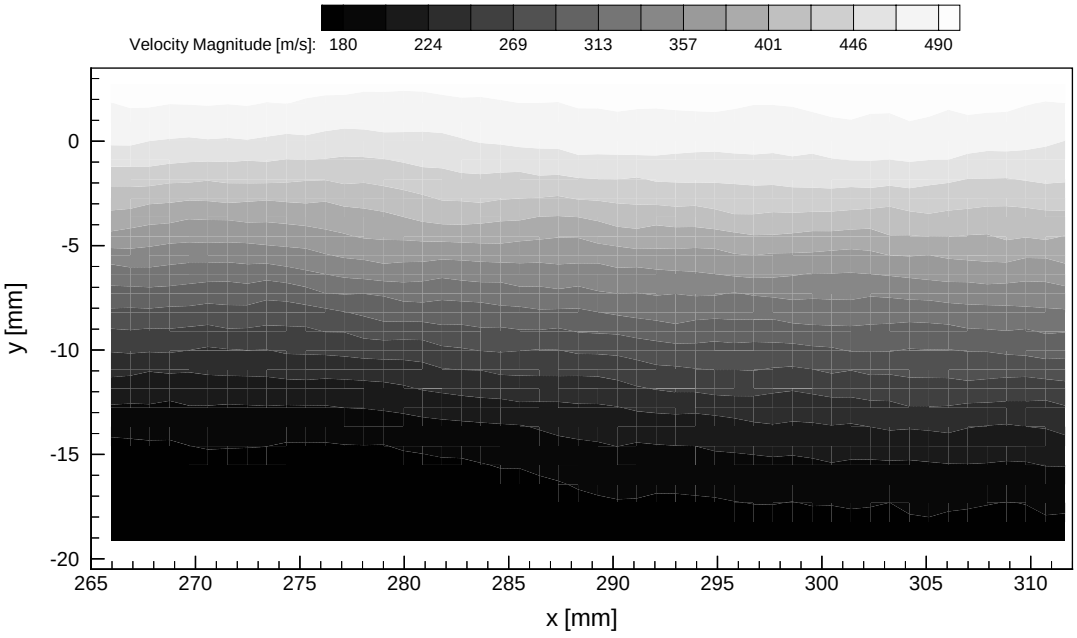

Figure 12: 100-frame average velocity magnitude: $M_c = 0.63$

a particular streamwise station frequently lie well within the envelope described by their excursions. That is, parcels of fluid retaining velocities near the freestream values penetrate well into the layer at certain streamwise locations. This high intermittency of velocity suggests that momentum exchange to and from freestream fluid occurs when it interacts with the structures already present in the layer, rather than when it enters the region demarcated by the time-averaged layer thickness.

Since the large-scale structures are a key feature of the turbulence of the mixing layer, and since they provide the reference point for evaluation of its compressibility, the velocity data are best evaluated in the frame of reference of the structures. For equal freestream specific heat ratios, the velocity of this convective frame is given by [26]:

$$U_c = \frac{a_2 U_1 + a_1 U_2}{a_1 + a_2} \tag{7}$$

which returns a value of 375 m/s for the present condition. Subtracting this value from the u velocity, we obtain the vector field given in Figure 8. Since the layer is compressible, the convective velocity is not the average of the freestream values; thus, in our convective frame the slow-stream velocity is smaller in absolute value than the fast-stream velocity. Locations of $u - U_c = 0$, marked by vertical vectors, wander over a 5–10-mm range, up to half the layer thickness; this reflects the diffuse, distorted nature of the large-scale structures observed in the scalar visualizations of the compressible case.

Despite marked irregularities of the instantaneous velocity field noted above, a 100-frame ensemble generates a smooth average, presented in Figures 9 and 10. The frame-averaged fields display the characteristic mixing-layer profile. We also observe finite values of v at the freestream interfaces due to entrainment, and a slight downward slope of the $u - U_c = 0$ line due to the streamwise growth of the layer into the low-speed stream.

Contour plots of velocity magnitude (Figures 11 and 12) provide a scalar format for the data. The instantaneous magnitude is reminiscent of scalar visualizations, with steep velocity gradients appearing to mark the boundaries of the large-scale structures. The presence of pockets or islands of low-speed fluid surrounded by high-speed fluid, and vice versa, is consistent with the three-dimensional nature of the compressible layer. Using a mixture fraction of 0.3, the sonic speed is estimated to be

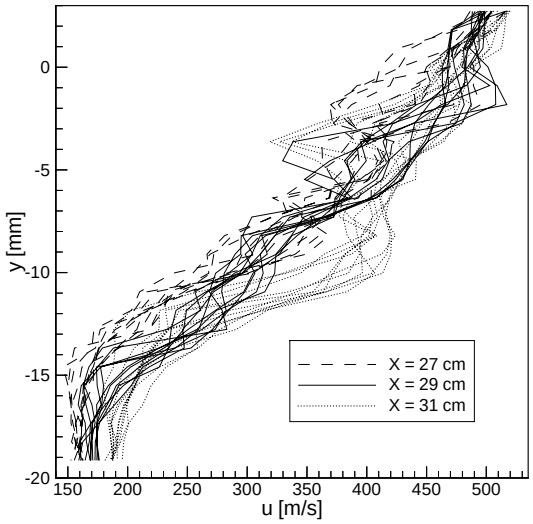

Figure 13: Instantaneous velocity profiles: $M_c = 0.63$

260 m/s; thus, the majority of the layer is seen to be supersonic.

Instantaneous u velocity profiles are presented in Figure 13, quantifying the intense streamwise variations observed in the vector fields. In the 100-frame ensemble (Figure 14), we confirm the recovery of the average. However, since Figure 14 is plotted in physical coordinates, we observe a gradual, monotonic streamwise variation in the profiles due to the growth of the layer. Since the layer grows asymmetrically toward the low-speed stream, its centerline descends across the imaged region (Figure 10). This results in a cross-stream shift as well as a change in scale of the profiles across the image. If we recast the data in similarity coordinates based on linear streamwise growth of δ, and measure y relative to the local layer centerline, the profiles collapse onto a single curve (Figure 15).

Conclusions

A PIV system for supersonic plane shear layers has been developed and validated, including an investigation of relevant seeding issues and leading to preliminary side-view velocity measurements in a turbulent, compressible flow having peak velocities over 500 m/s. For the compressible case ($M_c = 0.63, Re_\delta = 764,000$), the meandering nature of the instantaneous velocity field is revealed. The vector fields display spatial variations

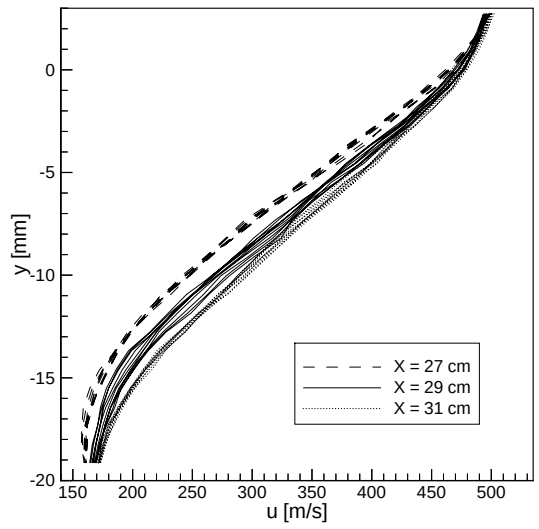

Figure 14: 100-frame average velocity profiles: $M_c = 0.63$

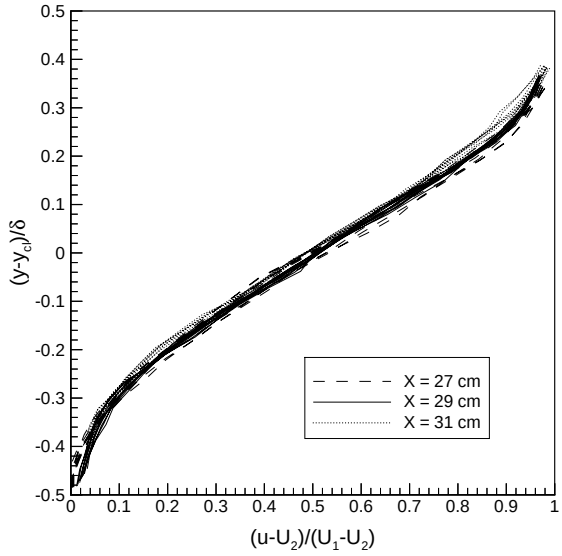

Figure 15: 100-frame average normalized velocity profiles: $M_c = 0.63$

suggesting that interaction with large-scale structures is an important mode of momentum transfer between newly-entrained fluid and that already mixing in the layer. Comparisons with previous LDV work, measurements at other compressibilities, plan views, and scalar visualization and structure velocimetry are important supplements to the work, and are presently being explored.

Acknowledgements

This work was supported by the Air Force Office of Scientific Research, J. Tishkoff Technical Monitor. WDU is supported by an AASERT grant. We would also like to thank E. F. Hasselbrink and L. Muñiz for help with the experiments.

References

[1] R. J. Adrian. Particle-imaging techniques for experimental fluid mechanics. *Annual Review of Fluid Mechanics*, 23:261–304, 1991.

[2] N. P. Cheremisinoff and P. N. Cheremisinoff. *Hydrodynamics of Gas-Solids Fluidization*. Gulf Publishing Company, 1984.

[3] N. T. Clemens and M. G. Mungal. Large-scale structure and entrainment in the supersonic mixing layer. *Journal of Fluid Mechanics*, 284:171–216, 1995.

[4] W. Crisler, A. Krothapalli, and L. Lourenço. PIV investigation of high speed flow over a pitching airfoil. AIAA paper 94-0533, 32nd Aerospace Sciences Meeting, Reno, NV, 1994.

[5] F. L. Crosswy. Particle size distributions of several commonly used seeding aerosols. In W. W. Hunter and C. E. Nichols, editors, *NASA CP 2393: Wind Tunnel Seeding Systems for Laser Velocimeters*, pages 53–75, 1985.

[6] G. S. Elliott and M. Samimy. Compressibility effects in free shear layers. *Physics of Fluids A*, 2:1231–1240, 1990.

[7] G. S. Elliott, M. Samimy, and G. S. Arnette. Study of compressible mixing layers using filtered Rayleigh scattering based visualizations. *AIAA Journal*, 30(10):2567–2569, 1992.

[8] G. S. Elliott, M. Samimy, and G. S. Arnette. The characteristics and evolution of

large-scale structures in compressible mixing layers. *Physics of Fluids*, 7:864–876, 1995.

[9] G. S. Elliott, M. Samimy, and S. A. Arnette. Details of a molecular filter-based velocimetry technique. AIAA paper 94-0490, 32nd Aerospace Sciences Meeting, Reno, NV, 1994.

[10] G. S. Elliott, M. Samimy, and S. A. Arnette. A molecular filter based velocimetry technique for high speed flows. *Experiments in Fluids*, 18:107–118, 1994.

[11] D. C. Fourguette, M. G. Mungal, and R. W. Dibble. Time evolution of the shear layer of a supersonic axisymmetric jet. *AIAA Journal*, 29:1123–1130, 1991.

[12] D. D. Glawe and M. Samimy. Dispersion of solid particles in compressible mixing layers. *Journal of Propulsion and Power*, 9(1):83–89, 1993.

[13] S. G. Goebel and J. C. Dutton. Experimental study of compressible turbulent mixing layers. *AIAA Journal*, 29(4):538–546, 1991.

[14] M. R. Gruber, N. L. Messersmith, and J. C. Dutton. Three-dimensional velocity field in a compressible mixing layer. *AIAA Journal*, 31:2061–2067, 1993.

[15] W. W. Hunter and C. E. Nichols, editors. *NASA CP 2393: Wind Tunnel Seeding Systems for Laser Velocimeters*, 1985.

[16] T. C. Island, W. D. Urban, and M. G. Mungal. Quantitative scalar measurements in compressible mixing layers. AIAA paper 96-0685, 34th Aerospace Sciences Meeting, Reno, NV, 1996.

[17] J. Kompenhans and R. Höcker. Application of particle image velocimetry to high speed flows. In *Particle Image Displacement Velocimetry*, pages 67–84. von Karman Institute for Fluid Dynamics, 1988.

[18] A. Krothapalli, D. P. Wishart, and L. M. Lourenço. Near field structure of a supersonic jet: "on-line" PIV study. In *Seventh International Symposium on Applications of Laser Techniques to Fluid Mechanics*, pages 26.5.1–26.5.6, 1994.

[19] J. Lepicovsky and R. J. Bruckner. Seeding for laser velocimetry in confined supersonic flows with shocks. In *Eighth International Symposium on Applications of Laser Techniques to Fluid Mechanics*, pages 15.1.1–15.1.9, 1996.

[20] A. Melling. Seeding gas flows for laser anemometry. In *AGARD CP-399: Conference on Advanced Instrumentation for Aero Engine Components*, pages 8.1–8.11, 1986.

[21] N. L. Messersmith, J. C. Dutton, and H. Krier. Experimental investigation of large scale structures in mixing layers. AIAA paper 91-0244, 29th Aerospace Sciences Meeting, Reno, NV, 1991.

[22] M. F. Miller, C. T. Bowman, and M. G. Mungal. The effects of compressibility on a turbulent reacting mixing layer. *Journal of Fluid Mechanics*, 1997. To appear.

[23] M. F. Miller, T. C. Island, J. M. Seitzman, C. T. Bowman, M. G. Mungal, and R. K. Hanson. An experimental investigation of supersonic reacting mixing layers. AIAA paper 94-0823, 32nd Aerospace Sciences Meeting, Reno, NV, 1993.

[24] M. J. Molezzi and J. C. Dutton. Application of particle image velocimetry in high speed separated flows. *AIAA Journal*, 31(3):438–446, 1993.

[25] D. Papamoschou. Structure of the compressible turbulent shear layer. AIAA paper 89-0126, 27th Aerospace Sciences Meeting, Reno, NV, 1989.

[26] D. Papamoschou and A. Roshko. The compressible turbulent shear layer: an experimental study. *Journal of Fluid Mechanics*, 197:453–477, 1988.

[27] W. P. Patrick. Overview of solid particle LV seeding techniques used at UTRC. In W. W. Hunter and C. E. Nichols, editors, *NASA CP 2393: Wind Tunnel Seeding Systems for Laser Velocimeters*, pages 105–113, 1985.

[28] J. Poggie and A. J. Smits. Large-scale coherent turbulence structures in a compressible mixing layer. AIAA paper 96-0440, 34th Aerospace Sciences Meeting, Reno, NV, 1996.

[29] M. Raffel, H. Höfer, F. Kost, C. Willert, and J. Kompenhans. Experimental aspects of PIV measurements of transonic flow fields at a trailing edge model of a turbine blade. In *Eighth International Symposium on Applications of Laser Techniques to Fluid Mechanics*, pages 28.1.1–28.1.10, 1996.

[30] C. Ross, L. Lourenço, and A. Krothapalli. Particle imaging velocimetry measurements in a shock-containing supersonic flow. AIAA paper 94-0047, 32nd Aerospace Sciences Meeting, Reno, NV, 1994.

[31] M. Samimy and B. A./K. Abu-Hijleh. Performance of laser Doppler velocimeter with polydisperse seed particles in high-speed flows. *Journal of Propulsion*, 5(1):21–25, 1989.

[32] J. M. Seitzman, M. F. Miller, T. C. Island, and R. K. Hanson. Double-pulse imaging using simultaneous OH/acetone PLIF for studying the evolution of high-speed, reacting mixing layers. In *Twenty-Fifth Symposium (International) on Combustion*, pages 1743–1750. The Combustion Institute, 1994.

[33] P. J. Strykowski, A. Krothapalli, and D. J. Forliti. Counterflow thrust vectoring of supersonic jets. AIAA paper 96-0115, 34th Aerospace Sciences Meeting, 1996.

[34] L. Svarovsky. Solid–gas separation. In M. Rhodes, editor, *Principles of Powder Technology*, pages 171–180. John Wiley and Sons, 1990.

[35] M. J. Walsh. Influence of particle drag coefficient on particle motion in high-speed flow with typical laser velocimeter applications. Technical Report NASA TN D-8120, NASA, 1976.

[36] Q. Wang and K. D. Squires. Particle transport in a nonuniformly seeded mixing layer. AIAA paper 96-0683, 34th Aerospace Sciences Meeting, Reno, NV, 1996.